Nanoscale

PAPER

View Article Online
View Journal | View Issue

Cite this: *Nanoscale*, 2016, **8**, 6629

Oxygen reduction catalyzed by gold nanoclusters supported on carbon nanosheets†

Qiannan Wang,‡[a] Likai Wang,‡[a] Zhenghua Tang,*[a,b] Fucai Wang,[c] Wei Yan,[a] Hongyu Yang,[a] Weijia Zhou,[a] Ligui Li,[a] Xiongwu Kang[a] and Shaowei Chen*[a,d]

Received 15th January 2016,
Accepted 23rd February 2016

DOI: 10.1039/c6nr00400h

www.rsc.org/nanoscale

Nanocomposites based on *p*-mercaptobenzoic acid-functionalized gold nanoclusters, $Au_{102}(p\text{-MBA})_{44}$, and porous carbon nanosheets have been fabricated and employed as highly efficient electrocatalysts for oxygen reduction reaction (ORR). $Au_{102}(p\text{-MBA})_{44}$ clusters were synthesized *via* a wet chemical approach, and loaded onto carbon nanosheets. Pyrolysis at elevated temperatures led to effective removal of the thiolate ligands and the formation of uniform nanoparticles supported on the carbon scaffolds. The nanocomposite structures were characterized by using a wide range of experimental techniques such as transmission electron microscopy, scanning electron microscopy, X-ray photoelectron spectroscopy, X-ray diffraction, UV-visible absorption spectroscopy, thermogravimetric analysis and BET nitrogen adsorption/desorption. Electrochemical studies showed that the composites demonstrated apparent ORR activity in alkaline media, and the sample with a 30% Au mass loading was identified as the best catalyst among the series, with a performance comparable to that of commercial Pt/C, but superior to those of Au_{102} nanoclusters and carbon nanosheets alone, within the context of onset potential, kinetic current density, and durability. The results suggest an effective approach to the preparation of high-performance ORR catalysts based on gold nanoclusters supported on carbon nanosheets.

Introduction

Developing effective energy technologies to eliminate our dependence on fossil fuels has been attracting a great deal of interest in recent decades. Towards this end, proton exchange membrane fuel cells represent a unique, promising alternative,[1–4] which entail two major reactions, oxidation of small organic molecule fuels at the anode and oxygen reduction at the cathode. Yet, because of the sluggish electron-transfer kinetics and complex reaction pathways, oxygen reduction reaction (ORR) at the cathode has long been recognized as a major bottleneck that impedes the fuel cell performance. Pt and Pt-based alloys have been used extensively as the catalysts of choice for ORR.[5–9] However, the limited reserves and high costs of Pt have significantly hampered the widespread commercial applications of fuel cells. Therefore, continuous efforts are urgently needed to develop readily available, cost-effective catalysts with activity comparable to or even better than that of commercial Pt/C.[10–18]

Within this context, gold nanoclusters have attracted particular attention as efficient catalysts for ORR, where strong core size effects have been observed.[19–21] However, gold nanoclusters are in general unstable and tend to dissolve and/or aggregate into larger particles during sample processing and electrochemical reactions.[20] To mitigate this issue, a variety of substrates have been used to support and stabilize gold nanoclusters, such as graphene,[21,22] mesoporous carbons,[23] TiO_2,[24] CeO_2,[25] and others.[26] Among these, carbon nanosheets represent a unique addition with a high surface area, excellent electrical conductivity, and robust electrochemical stability.[27] This is the primary motivation of the present study.

In this study, nanocomposites based on *p*-mercaptobenzoic acid-functionalized Au_{102} nanoclusters, $Au_{102}(p\text{-MBA})_{44}$, and porous carbon nanosheets have been fabricated and employed as highly efficient electrocatalysts for ORR. The gold nanoclusters were prepared by a wet chemical method and loaded onto carbon nanosheets. Pyrolysis at controlled temperatures (600 °C) led to effective removal of the organic capping ligands such that gold nanoparticles were in intimate contact with the carbon scaffolds. Electrochemical studies of the resulting

[a]*New Energy Research Institute, School of Environment and Energy, South China University of Technology, Guangzhou Higher Education Mega Centre, Guangzhou, 510006, P. R. China. E-mail: zhht@scut.edu.cn*
[b]*Guangdong Provincial Key Laboratory of Atmospheric Environment and Pollution Control, Guangzhou, Guangdong 510006, P. R. China*
[c]*Zijin Mining Group Co. Ltd, Shanghang, Fujian 364200, P. R. China*
[d]*Department of Chemistry and Biochemistry, University of California, 1156 High Street, Santa Cruz, California 95064, USA. E-mail: shaowei@ucsc.edu*
† Electronic supplementary information (ESI) available: Additional experimental data and discussion. See DOI: 10.1039/c6nr00400h
‡ These authors contributed.

nanocomposites demonstrated excellent ORR activity in alkaline media, and the sample with a 30% Au mass loading exhibited the highest activity among the series, a performance comparable to that of commercial Pt/C.

Experimental section

Materials

Hydrogen tetrachloroauric acid(III) trihydrate ($HAuCl_4{\cdot}3H_2O$, 98%, Energy Chemicals, Shanghai), *p*-mercaptobenzoic acid (*p*-MBA, 90%, Energy Chemicals, Shanghai), terephthalic acid (99.99%, Aladdin Industrial Corporation, Shanghai), sodium borohydride ($NaBH_4$, 98%, Aladdin Industrial Corporation, Shanghai), Pt/C (20 wt%, Alfa Aesar), zinc nitrate hexahydrate ($Zn(NO_3)_2{\cdot}6H_2O$, 99%, Fuchen Reagents, Tianjin), ammonium acetate (NH_4OAc, 98%, Fuchen Reagents, Tianjin), cetyltrimethylammonium bromide (CTAB, 99%, Fuchen Reagents, Tianjin), triethylamine (TEA, 99%, Fuchen Reagents, Tianjin), methanol (99.5%, Xinyun Chemical Industry, Tianjin), and *N*,*N*-dimethylformamide (DMF, 99.5%, Fuchen Reagents, Tianjin) were used as received. Water was supplied by a Barnstead Nanopure Water System (18.3 MΩ cm).

Preparation of carbon nanosheets

Carbon nanosheets were prepared by adopting a protocol reported previously.[28,29] In a typical reaction, 17.95 g of $Zn(NO_3)_2{\cdot}6H_2O$ and 3.325 g of terephthalic acid were co-dissolved in 500 mL of DMF in a round bottom flask, and aged at 333 K for 72 h. 0.1 mol of CTAB (36.4 g) were then dissolved into the solution under magnetic stirring. The subsequent addition of TEA (0.1 mol, 13.9 mL) into the solution led to the formation of a precipitate, which was collected by centrifugation with the addition of a large amount of DMF and chloroform. The precipitate was then dried in vacuum at 432 K for 24 h before being loaded onto a ceramic boat for carbonization under a nitrogen flow at 900 °C for 6 h, affording carbon nanosheets, as manifested in TEM and SEM measurements (Fig. S1†). From nitrogen adsorption/desorption measurements (Fig. S2†), the specific surface area of the carbon nanosheets was estimated to be 1413.7 $m^2\ g^{-1}$ with an average pore size of 4.0 ± 0.7 nm.

Synthesis of Au_{102}(*p*-MBA)$_{44}$ nanoclusters

Au_{102}(*p*-MBA)$_{44}$ nanoclusters were synthesized by following the procedure reported earlier.[30] Briefly, 2.57 mL of 28 mM $HAuCl_4{\cdot}3H_2O$, 11.28 mL of methanol and 2.27 mL of a solution containing 95 mM *p*-MBA and 300 mM NaOH were mixed with 7.88 mL of H_2O in a 100 mL round bottom flask, corresponding to a 3 : 1 molar feed ratio of *p*-MBA to $HAuCl_4$. The solution was under magnetic stirring for 1 h at room temperature when it became light yellow. Then 0.96 mL of a freshly prepared $NaBH_4$ aqueous solution was added rapidly (at a 2 : 1 molar ratio of $NaBH_4$: Au) under vigorous stirring, where the solution color was found to change to deep red brown instantly, signifying the formation of gold nanoclusters. After magnetic stirring overnight at room temperature, the nanoclusters were collected by centrifugation with the addition of 80 mM NH_4OAc and 80% v/v methanol, and dried in air overnight. The samples were then re-dissolved in 0.4 mL of water. Large clusters were removed by centrifugation with the addition of 0.12 M NH_4OAc and 60% v/v of methanol. The supernatant was collected, into which was added a large access of NH_4OAc (final concentration 0.12 M) and methanol (80%), leading to the formation of a precipitate which was the molecular Au_{102}(*p*-MBA)$_{44}$ clusters. The average diameter was estimated to be 1.17 ± 0.26 nm, as determined by transmission electron microscopic measurements (Fig. S3†), and thermogravimetric analysis showed about 25.01% of organic components (Fig. S4†), both of which were consistent with the literature data of Au_{102}(*p*-MBA)$_{44}$ nanoclusters (Fig. S5 and S6†).[30–34]

Preparation of carbon nanosheets-supported gold clusters (AuCNS)

The preparation scheme is depicted in Fig. 1. In a typical reaction, 20 mg of carbon nanosheets obtained above was dispersed in 150 mL of H_2O in a glass beaker. Separately, 11.46 mg of the Au_{102}(*p*-MBA)$_{44}$ clusters (corresponding to a Au mass of 8.57 mg) was added into 20 mL of H_2O under magnetic stirring for 20 min. The gold cluster solution was then added dropwise into the carbon nanosheets solution under vigorous stirring and sonicated for 3 h at room temperature. Solvents were then removed by rotary evaporation, and the remaining solids were collected and pyrolyzed under a nitrogen flow at 600 °C for 2 h, affording a gold nanoclusters/carbon nanosheets nanocomposite at a 30% mass loading of Au (denoted as AuCNS-30%). Samples at other Au mass loadings (10, 20 and 40%) were prepared in a similar fashion, which were denoted as AuCNS-10%, -20% and -40%, respectively.

Characterizations

UV-visible absorption spectra were obtained with a Shimadzu 2600/2700 UV-visible scanning spectrophotometer using a

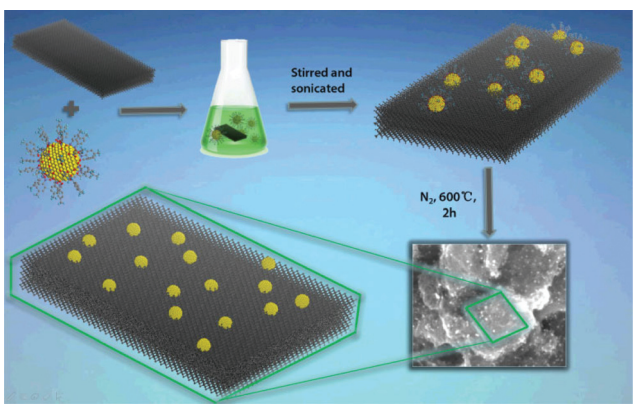

Fig. 1 Schematic illustration of the preparation of nanocomposites based on Au_{102} nanoclusters supported on carbon nanosheets.

1 cm quartz cuvette. TEM micrographs were acquired with a high-resolution transmission electron microscope (JEOL JEM-2010), where samples were prepared by dropcasting a catalyst dispersion directly onto a copper grid coated with a holey carbon film. Field-emission scanning electron microscopic (FESEM, NOVA NanoSEM 430, FEI) measurements were employed to characterize the surface morphologies of the as-prepared samples. Samples for FESEM analysis were prepared by dispensing several drops of the dilute catalyst dispersion in ethanol on a clean silicon (111) substrate. BET surface areas were determined with a Micromeritics ASAP 2010 instrument with nitrogen adsorption at 77 K using the Barrett–Joyner–Halenda (BJH) method. The pore-size distribution was calculated with a DFT method by using the nitrogen adsorption/desorption isotherm and assuming a slit pore model. X-ray diffraction (XRD) patterns in the Bragg's angle (2θ) range of 20 to 80° were collected at room temperature by using a Bruker D8 diffractometer with Cu K_α radiation (λ = 0.1541 nm). X-ray photoelectron spectroscopy (XPS) analysis was conducted with a VG MultiLab 2000 instrument with a monochromatic Al K_α X-ray source (Thermo VG Scientific). Thermogravimetric analysis (TGA) was performed on a METTLER instruments under a N_2 atmosphere at a heating rate of 5 °C min^{-1}.

Electrochemical measurements

Electrochemical measurements were carried out with a CHI 750E electrochemical workstation (CH Instruments Inc.) in a 0.1 M KOH aqueous solution at room temperature. A platinum wire and a Ag/AgCl electrode were used as the counter electrode and reference electrode, respectively. The working electrode was a glassy carbon disk electrode (diameter 5.61 mm) of an RRDE (with a collection efficiency of 37%) from Pine Instrument, Inc. The working electrode was cleaned by mechanical polishing with aqueous slurries of 0.3 μm alumina powders on a polishing microcloth. The catalyst ink was prepared by adding 2 mg of a catalyst into 1.0 mL ethanol solution containing 10 μL Nafion (5 wt%, Aldrich). 10 μL of the catalyst ink was then dropcast onto the glassy carbon disk and dried at room temperature, and the catalyst loading was calculated to be 80.8 μg cm^{-2} for all samples. In all measurements, the Ag/AgCl reference electrode was calibrated with respect to a reversible hydrogen electrode (RHE).The calibration was performed in a high-purity H_2 (99.999%) saturated electrolyte with a Pt wire as both the working electrode and counter electrode. Cyclic voltammograms were collected at a scan rate of 10 mV s^{-1}, and the average of the two potentials at which the current crossed zero was taken as the thermodynamic potential of the RHE. In 0.1 M KOH, $E_{Ag/AgCl} = E_{RHE} + 0.966$ V.

Results and discussion

As depicted in Fig. 1, AuCNS nanocomposites were prepared by loading $Au_{102}(p\text{-MBA})_{44}$ nanoclusters onto carbon nanosheets, followed by pyrolysis at controlled temperatures. Fig. 2 shows representative TEM images of the AuCNS-10%, 20%, 30% and 40% samples, as well as their corresponding core size histograms. One can see that even after calcination at elevated temperatures, gold nanoclusters remained well dispersed, without apparent aggregation (see also Fig. S7†). Yet the average core diameters were somewhat greater than that of the as-prepared $Au_{102}(p\text{-MBA})_{44}$ nanoclusters (Fig. S3†), 2.10 ± 0.43 nm for AuCNS-10%, 2.56 ± 0.69 nm for AuCNS-20%, 2.59 ± 0.70 nm for AuCNS-30%, and 4.80 ± 1.64 nm for AuCNS-40%, increasing with increasing gold loading.

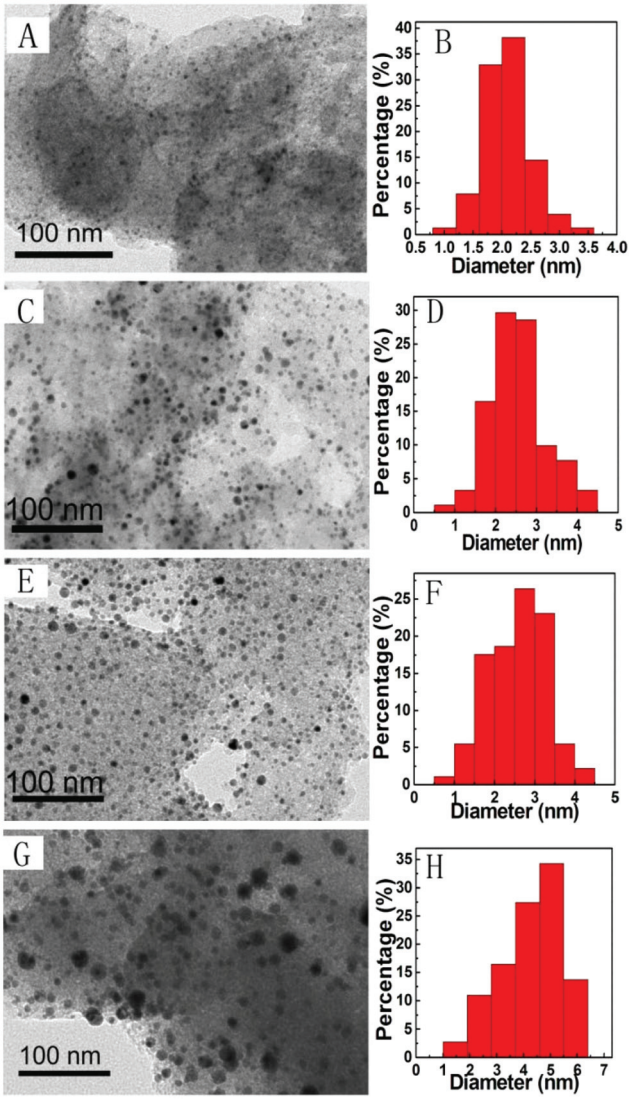

Fig. 2 Representative TEM image and corresponding core size histogram of (a, b) AuCNS-10%, (c, d) AuCNS-20%, (e, f) AuCNS-30%, and (g, h) AuCNS-40%.

The structures of the AuCNS nanocomposites were then examined by XRD measurements. As depicted in Fig. 3a, two diffraction peaks can be seen at 2θ = 29.1 and 42.5°, which may be assigned to the (002) and (101) crystalline planes of hexagonal carbon (JCPDS 75-1621), respectively. For AuCNS-30%, four additional diffraction peaks also emerged at 2θ = 38.1°, 44.2°, 64.7°, and 77.8°, in agreement with the (111),

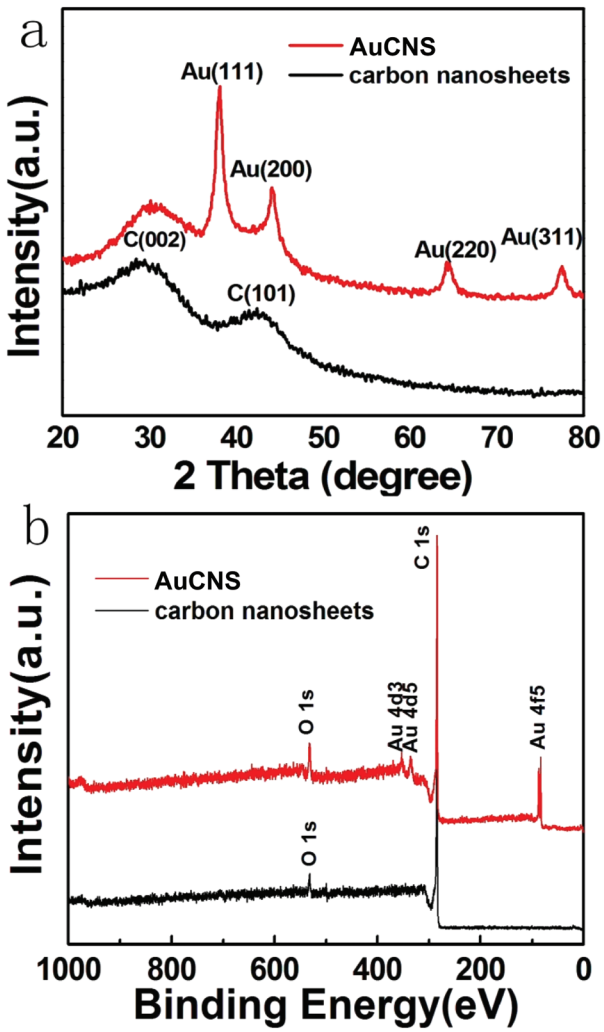

Fig. 3 (a) XRD patterns and (b) XPS survey spectra of AuCNS-30% and carbon nanosheets.

(200), (220) and (311) diffractions of fcc gold (JCPDS 75-2870).[35] Consistent results were obtained in XPS measurements. From Fig. 3b, Au 4d (~345 eV) and Au 4f (85 eV) electrons can be readily identified for the AuCNS-30% sample, along with the C 1s (285 eV) and O 1s (532 eV) peaks that arose from carbon nanosheets, confirming the effective loading of gold nanoclusters onto the carbon substrates. The XPS survey spectra of other AuCNS samples can be found in Fig. S8.† Based on the integrated peak areas, the Au contents in these composites were calculated to be 1.2 at% (AuCNS-10%), 1.9 at% (AuCNS-20%), 2.5 at% (AuCNS-30%) and 3.1 at% (AuCNS-40%).

Fig. S9† depicts the high-resolution XPS scans of the Au 4f electrons of $Au_{102}(p\text{-MBA})_{44}$, AuCNS-10%, AuCNS-20%, AuCNS-30%, and AuCNS-40%. For the $Au_{102}(p\text{-MBA})_{44}$ nanoclusters, the binding energy of Au $4f_{7/2}$ electrons can be estimated to be 84.4 eV, which is in the intermediate between those of Au(0) (83.8 eV) and Au(I) (85.0–86.0 eV), likely due to the nanometer size and incomplete coordination of the cluster cores, as compared to the bulk counterparts.[33,36] In fact, for the AuCNS composites, with increasing gold loading (and nanoparticle core size, Fig. 2), one can see that the binding energy of the Au $4f_{7/2}$ electrons decreased from 84.3 eV for AuCNS-10% to 84.0 eV for AuCNS-40%. From the high-resolution scans of the C 1s electrons (Fig. S10†), three components can be identified by peak deconvolution, sp_2 C at 284.8 eV, C in C–O at 286.4 eV, and the carbonyl C at 287.8 eV. Interestingly, the binding energy of carbonyl C in the AuCNS samples was about 0.6 eV higher than that in carbon nanosheets alone, suggesting that the carbonyl C might be involved in the formation of gold carboxylate moieties ($Au–COO^-$) with relatively strong electronic interactions.[37,38]

The electrocatalytic activity towards ORR of the AuCNS samples was then examined and compared by voltammetric measurements. As shown in Fig. 4a, whereas only featureless double-layer charging current was observed in N_2-saturated 0.1 M KOH within the potential range of −0.04 V to +1.16 V, a cathodic peak can be readily identified when the solution was saturated with oxygen, suggesting effective electrocatalytic activity for oxygen reduction. The AuCNS-30% modified electrode displayed an apparent cathodic peak at +0.85 V (*vs.* RHE), markedly more positive than that of commercial Pt/C catalyst (+0.81 V), whereas the peak current density was the same at 0.57 mA cm^{-2}, indicating highly comparable ORR activity. Consistent behaviors can be seen in RRDE voltammetric measurements, as depicted in Fig. 4b. The onset potential (E_{onset}) was about +0.96 V for AuCNS-30%, and +0.97 V for commercial Pt/C; and the diffusion limited current density (at +0.45 V and 2500 rpm) was 3.96 mA cm^{-2} for AuCNS-30%, somewhat lower than that of commercial Pt/C catalyst (4.98 mA cm^{-2}).

Next, based on the RRDE data (Fig. 4b), the number of electron transfer (n) and the H_2O_2 percent yield in ORR can also be quantified by $n = \frac{4I_d}{I_d + I_r/N}$ and $H_2O_2 = \frac{200I_r/N}{\frac{I_r}{N} + I_d}$, where I_d is the disk current, I_r is the ring current, and N is the RRDE collection efficiency (0.37). From Fig. 4c one can see that within the wide potential range of +0.20 to +0.80 V, the n values were 3.50–3.86 for AuCNS-30%, very close to those of Pt/C (n = 3.70–3.88). Correspondingly, the H_2O_2 yield for AuCNS-30% was <20% in the low overpotential range of +0.50 to +0.80 V, as compared to less than 10% for Pt/C. These results, again, indicate that AuCNS-30% behaved similarly to Pt/C in the (almost) complete reduction of oxygen to water.

Fig. 4d shows the RRDE voltammograms of oxygen reduction recorded at the AuCNS-30% electrode in an oxygen-saturated 0.1 M KOH solution at different rotation rates (from 100 to 2500 rpm). It can be seen that the voltammetric currents increased when increasing electrode rotation rate, and the corresponding Koutecky–Levich plots (Fig. 4e) within the potential range of +0.67 to +0.88 V exhibit good linearity with a rather consistent slope, suggesting first order reaction kinetics of ORR with respect to oxygen concentration in the solution. The corresponding Tafel plots are depicted in Fig. 4f, where a similar slope was observed for AuCNS-30% (63 mV dec^{-1}) and

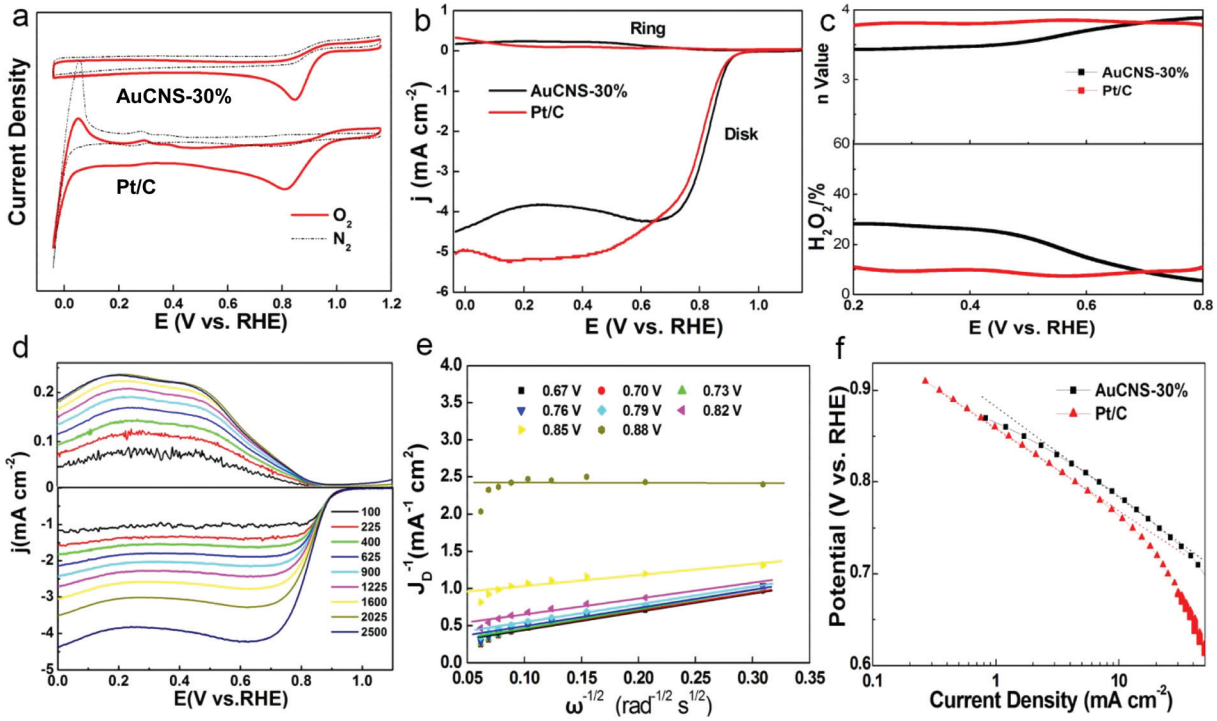

Fig. 4 (a) Cyclic and (b) RRDE voltammograms, (c) plots of H_2O_2 yield and number of electron transfer of a glassy carbon electrode modified with AuCNS-30% and commercial Pt/C catalyst in O_2-saturated 0.1 M KOH. Statistic results were based on data of three independent measurements. (d) LSV curves for AuCNS-30% at the rotation rates of 100 to 2500 rpm. (e) The corresponding K–L plots for AuCNS-30% at different electrode potentials. (f) The corresponding Tafel plots of AuCNS-30% and commercial Pt/C catalyst. All measurements were conducted at a catalyst loading of 80.8 μg cm^{-2} in an O_2 saturated 0.1 M KOH aqueous solution at a potential weep rate of 10 mV s^{-1}.

Pt/C (58.5 mV dec^{-1}), suggesting a similar reaction mechanism of ORR on the catalyst surface where the rate-determining step at both catalysts was likely the first electron reduction of oxygen.

The effects of Au loading in the nanocomposites on the ORR performance were then investigated by RRDE voltammetric measurements. Fig. 5 shows the RRDE voltammograms of a glassy carbon disk electrode modified with AuCNS-10%, AuCNS-20%, AuCNS-30% and AuCNS-40% in an oxygen-saturated 0.1 M KOH solution at a rotation speed of 2500 rpm. It can be seen that in all samples nonzero cathodic currents started to appear when the electrode potential was swept negatively to about +0.9 V and reached a plateau at potentials more negative than +0.7 V, suggesting apparent electrocatalytic activity of the nanocomposites in oxygen reduction. In addition, the voltammetric currents collected at the ring electrode, were about an order of magnitude lower, which indicated that only a minimal amounts of peroxide intermediates were produced during oxygen reduction. Yet a careful examination suggests that the catalytic performance actually varies rather drastically with the Au loading. For instance, the onset potential and diffusion-limited currents (at +0.55 V and 2500 rpm) of the series can be estimated to be +0.91 V and 3.95 mA cm^{-2} for AuCNS-10%, +0.93 V and 3.86 mA cm^{-2} for AuCNS-20%, +0.96 V and 4.20 mA cm^{-2} for AuCNS-30%, +0.90 V and 3.96 mA cm^{-2} for AuCNS-40%, respectively. That is, the sample with a 30% Au mass loading exhibited the best electrocatalytic activity among the series. Consistent results can be seen in cyclic voltammetric measurements (Fig. S11†). This is

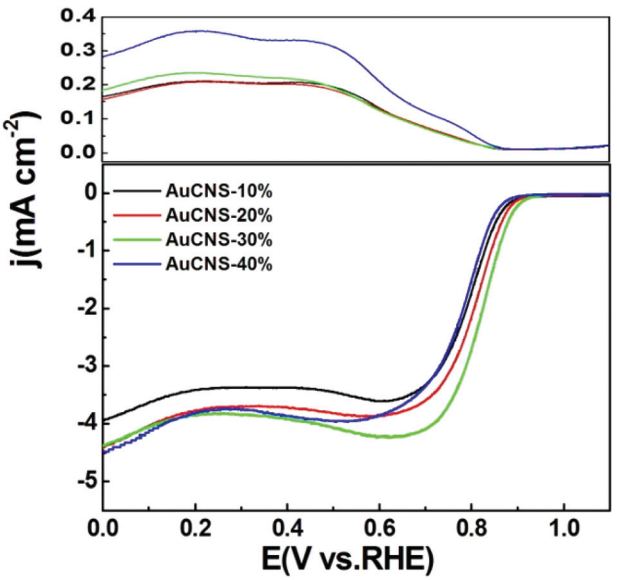

Fig. 5 RRDE voltammograms measurements of AuCNS-10%, AuCNS-20%, AuCNS-30%, and AuCNS-40%, in O_2-saturated 0.1 M KOH at 2500 rpm.

likely due a delicate balance between the Au loading and effective surface area. In principle, the number of active sites in the AuCNS nanocomposites would increase with increasing gold loading. Yet, at high gold concentrations, agglomeration of the gold nanoparticles most likely occurs, leading to reduced accessibility of the electrocatalytically active sites and hence diminished ORR activity.

It should be noted that the ORR activity of AuCNS is actually markedly better than that of carbon nanosheets or Au_{102}(*p*-MBA)$_{44}$ nanoclusters alone (Fig. S12†). The remarkable electrocatalytic performance may be interpreted by the following accounts. First of all, it has been reported that the ultrasmall size of the gold clusters is beneficial for the activation of molecular oxygen because of a decrease of the activation energy in the dissociative chemisorption of molecular oxygen, which facilitates the 4-electron reduction of oxygen.[19,20,39,40] Second, in the AuCNS nanocomposites, the carbon nanosheets not only served as a support, but also played an important role in the electronic interactions with the gold clusters, as evidenced in XPS measurements (Fig. 2, S9 and S10†). Such interactions might markedly impede the migration and fusion of Au clusters on the carbon surface leading to improved catalyst stability during the ORR process. In fact, strong gold–carbon interactions have been reported to play a key role in the catalytic reactions of propene epoxidation and hydrogen dissociation.[41,42] Moreover, the intimate synergistic interactions between the gold nanoparticles and carbon supports may also decrease the energy barrier of the rate-determining step by reducing the stability of ORR intermediate species.[22]

Finally, the durability of AuCNS-30% and commercial Pt/C for ORR was also evaluated and compared by chronoamperometric measurements. As depicted in Fig. 6, after more than 8 h's continuous operation, the cathodic current of the commercial Pt/C catalyst exhibited a clear loss of 35% of the initial value, whereas AuCNS-30% retained about 75% of its initial current under the same experimental conditions. This suggests improved stability of AuCNS as compared to Pt/C. In fact, the ORR performance of AuCNS-30% was virtually invariant when the catalysts were recycled and tested 3 times (Fig. S13†).

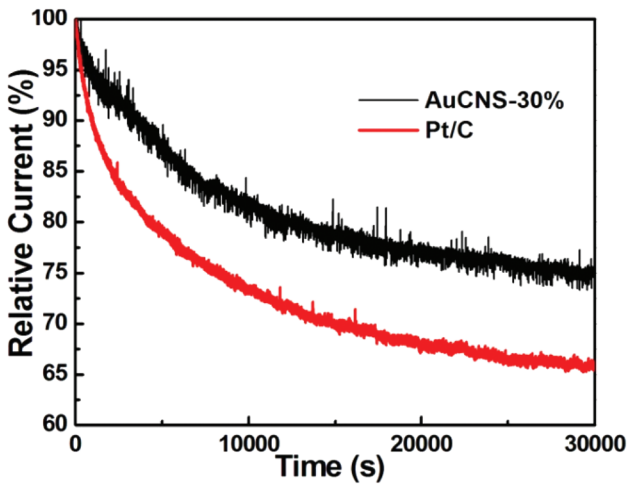

Fig. 6 Chronoamperometric responses for ORR at AuCNS-30% and Pt/C electrodes in an O_2-saturated 0.1 M KOH solution at +0.5 V for 30 000 s.

Conclusions

In summary, nanocomposites based on gold nanoclusters supported on carbon nanosheets were prepared by pyrolysis at controlled temperatures. The samples exhibited apparent electrocatalytic activity towards ORR in alkaline media, a performance highly comparable to that of commercial Pt/C but markedly better than the carbon nanosheets or the gold nanoclusters alone. The sample with a 30% Au mass loading was identified as the best catalyst among the series, in terms of onset potential, kinetic current density, and stability. The results highlight the significance of nanoengineered gold–carbon hybrids in the electrocatalytic reduction of oxygen.

Acknowledgements

This work was supported by the National Recruitment Program of Global Experts and the National Natural Science Foundation of China (no. 21528301 and 21501059). Z. H. T. also acknowledges financial support from the Fundamental Research Funds for the Central Universities (SCUT Grant No. 2015ZM012 and 2015PT026), and Guangdong Natural Science Funds for Distinguished Young Scholars (no. 2015A030306006). S. W. C. also thanks the National Science Foundation for partial support of the work (CHE-1265635 and DMR-1409396).

References

1 M. K. Debe, *Nature*, 2012, **486**, 43–51.
2 A. Kraytsberg and Y. Ein-Eli, *Energy Fuels*, 2014, **28**, 7303–7330.
3 K. E. Swider-Lyons and S. A. Campbell, *J. Phys. Chem. Lett.*, 2013, **4**, 393–401.
4 A. A. Gewirth and M. S. Thorum, *Inorg. Chem.*, 2010, **49**, 3557–3566.
5 S. Guo, S. Zhang and S. Sun, *Angew. Chem., Int. Ed.*, 2013, **52**, 8526–8544.
6 C.-H. Cui and S.-H. Yu, *Acc. Chem. Res.*, 2013, **46**, 1427–1437.
7 B. Lim, M. Jiang, P. H. C. Camargo, E. C. Cho, J. Tao, X. Lu, Y. Zhu and Y. Xia, *Science*, 2009, **324**, 1302–1305.
8 Y. Bing, H. Liu, L. Zhang, D. Ghosh and J. Zhang, *Chem. Soc. Rev.*, 2010, **39**, 2184–2202.
9 Y. Kang, X. Ye, J. Chen, Y. Cai, R. E. Diaz, R. R. Adzic, E. A. Stach and C. B. Murray, *J. Am. Chem. Soc.*, 2013, **135**, 42–45.
10 G. Wu and P. Zelenay, *Acc. Chem. Res.*, 2013, **46**, 1878–1889.

11 M. Liu, R. Zhang and W. Chen, *Chem. Rev.*, 2014, **114**, 5117–5160.
12 W. Ding, L. Li, K. Xiong, Y. Wang, W. Li, Y. Nie, S. Chen, X. Qi and Z. Wei, *J. Am. Chem. Soc.*, 2015, **137**, 5414–5420.
13 K. Zhou, W. Zhou, X. Liu, Y. Wang, J. Wan and S. Chen, *ACS Appl. Mater. Interfaces*, 2014, **6**, 14911–14918.
14 W. Niu, L. Li, X. Liu, N. Wang, J. Liu, W. Zhou, Z. Tang and S. Chen, *J. Am. Chem. Soc.*, 2015, **137**, 5555–5562.
15 H.-W. Liang, W. Wei, Z.-S. Wu, X. Feng and K. Müllen, *J. Am. Chem. Soc.*, 2013, **135**, 16002–16005.
16 J. Liang, X. Du, C. Gibson, X. W. Du and S. Z. Qiao, *Adv. Mater.*, 2013, **25**, 6226–6231.
17 Q. Wang, Z.-Y. Zhou, Y.-J. Lai, Y. You, J.-G. Liu, X.-L. Wu, E. Terefe, C. Chen, L. Song, M. Rauf, N. Tian and S.-G. Sun, *J. Am. Chem. Soc.*, 2014, **136**, 10882–10885.
18 K. P. Singh, E. J. Bae and J.-S. Yu, *J. Am. Chem. Soc.*, 2015, **137**, 3165–3168.
19 W. Chen and S. Chen, *Angew. Chem., Int. Ed.*, 2009, **48**, 4386–4389.
20 W. Tang, H. Lin, A. Kleiman-Shwarsctein, G. D. Stucky and E. W. McFarland, *J. Phys. Chem. C*, 2008, **112**, 10515–10519.
21 G. Goncalves, P. A. A. P. Marques, C. M. Granadeiro, H. I. S. Nogueira, M. K. Singh and J. Grácio, *Chem. Mater.*, 2009, **21**, 4796–4802.
22 H. Yin, H. Tang, D. Wang, Y. Gao and Z. Tang, *ACS Nano*, 2012, **6**, 8288–8297.
23 L. Wang, Z. Tang, X. Liu, W. Niu, K. Zhou, H. Yang, W. Zhou, L. Li and S. Chen, *RSC Adv.*, 2015, **5**, 103421–103427.
24 C. Lin, Y. Song, L. Cao and S. Chen, *ACS Appl. Mater. Interfaces*, 2013, **5**, 13305–13311.
25 J. Qi, J. Chen, G. Li, S. Li, Y. Gao and Z. Tang, *Energy Environ. Sci.*, 2012, **5**, 8937–8941.
26 C. Jin, X. Cao, F. Lu, Z. Yang and R. Yang, *ACS Appl. Mater. Interfaces*, 2014, **6**, 847–853.
27 H. Fan and W. Shen, *ChemSusChem.*, 2015, **8**, 2004–2027.
28 M. Ma, D. Zacher, X. Zhang, R. A. Fischer and N. Metzler-Nolte, *Cryst. Growth Des.*, 2011, **11**, 185–189.
29 T. Yoskamtorn, S. Yamazoe, R. Takahata, J.-i. Nishigaki, A. Thivasasith, J. Limtrakul and T. Tsukuda, *ACS Catal.*, 2014, **4**, 3696–3700.
30 Y. Levi-Kalisman, P. D. Jadzinsky, N. Kalisman, H. Tsunoyama, T. Tsukuda, D. A. Bushnell and R. D. Kornberg, *J. Am. Chem. Soc.*, 2011, **133**, 2976–2982.
31 M.-C. Daniel and D. Astruc, *Chem. Rev.*, 2004, **104**, 293–346.
32 O. Varnavski, G. Ramakrishna, J. Kim, D. Lee and T. Goodson, *J. Am. Chem. Soc.*, 2010, **132**, 16–17.
33 Z. Tang, D. A. Robinson, N. Bokossa, B. Xu, S. Wang and G. Wang, *J. Am. Chem. Soc.*, 2011, **133**, 16037–16044.
34 A. Dass, R. Guo, J. B. Tracy, R. Balasubramanian, A. D. Douglas and R. W. Murray, *Langmuir*, 2008, **24**, 310–315.
35 H. Qian and R. Jin, *Nano Lett.*, 2009, **9**, 4083–4087.
36 M. J. Hostetler, J. E. Wingate, C. J. Zhong, J. E. Harris, R. W. Vachet, M. R. Clark, J. D. Londono, S. J. Green, J. J. Stokes, G. D. Wignall, G. L. Glish, M. D. Porter, N. D. Evans and R. W. Murray, *Langmuir*, 1998, **14**, 17–30.
37 J.-W. Park and J. S. Shumaker-Parry, *ACS Nano*, 2015, **9**, 1665–1682.
38 J.-W. Park and J. S. Shumaker-Parry, *J. Am. Chem. Soc.*, 2014, **136**, 1907–1921.
39 G. He, Y. Song, K. Liu, A. Walter, S. Chen and S. Chen, *ACS Catal.*, 2013, **3**, 831–838.
40 Y. Song and S. Chen, *ACS Appl. Mater. Interfaces*, 2014, **6**, 14050–14060.
41 J. Huang, T. Akita, J. Faye, T. Fujitani, T. Takei and M. Haruta, *Angew. Chem., Int. Ed.*, 2009, **48**, 7862–7866.
42 T. Fujitani, I. Nakamura, T. Akita, M. Okumura and M. Haruta, *Angew. Chem., Int. Ed.*, 2009, **48**, 9515–9518.